

Supplementary File S1. Detailed description of the material, methods, and results of

The latest freshwater giants: a new *Peltocephalus* (Pleurodira: Podocnemididae) turtle from the Late Pleistocene of the Brazilian Amazon

Ferreira GS*, Nascimento ER, Cadena EA, Cozzuol MA, Farina BM, Pacheco MLAF, Rizzutto MA, Langer MC

*corresponding author: gabriel.ferreira@senckenberg.de

Contents of Supplementary File S1

MATERIALS & METHODS	2
GEOLOGICAL CONTEXT	2
SPECIMENS ANALYSED AND MEASUREMENTS	2
MICRO-COMPUTED TOMOGRAPHY (μ CT) OF EXTANT TAXA	4
MORPHOMETRIC COMPARISONS AND SIZE ESTIMATION	5
^{14}C RADIOCARBON AND STABLE ISOTOPE RATIO $\Delta^{13}\text{C}$ ANALYSES	6
SAMPLING FOR SPECTROSCOPIC ANALYSIS	7
MICRO-RAMAN SPECTROSCOPY.....	7
ENERGY DISPERSIVE X-RAY FLUORESCENCE (EDXRF)	7
RESULTS	8
GEOCHEMICAL AND RADIOCARBON DATING ANALYSES	8
COMPARATIVE DESCRIPTION	14
MORPHOSPACE ANALYSIS	17
BODY SIZE ESTIMATION	19
SUPPLEMENTARY REFERENCES.....	20

List of Supplementary Files:

Suppl_File_S1: Detailed description of the material, methods, and results
Suppl_File_S2: morphometric dataset
Suppl_File_S3: body size dataset
Suppl_File_S4: size corrected and log-transformed morphometric dataset
Suppl_File_S5: Micro-Raman raw data
Suppl_File_S6: EDXRF raw data counts
Suppl_File_S7: R script

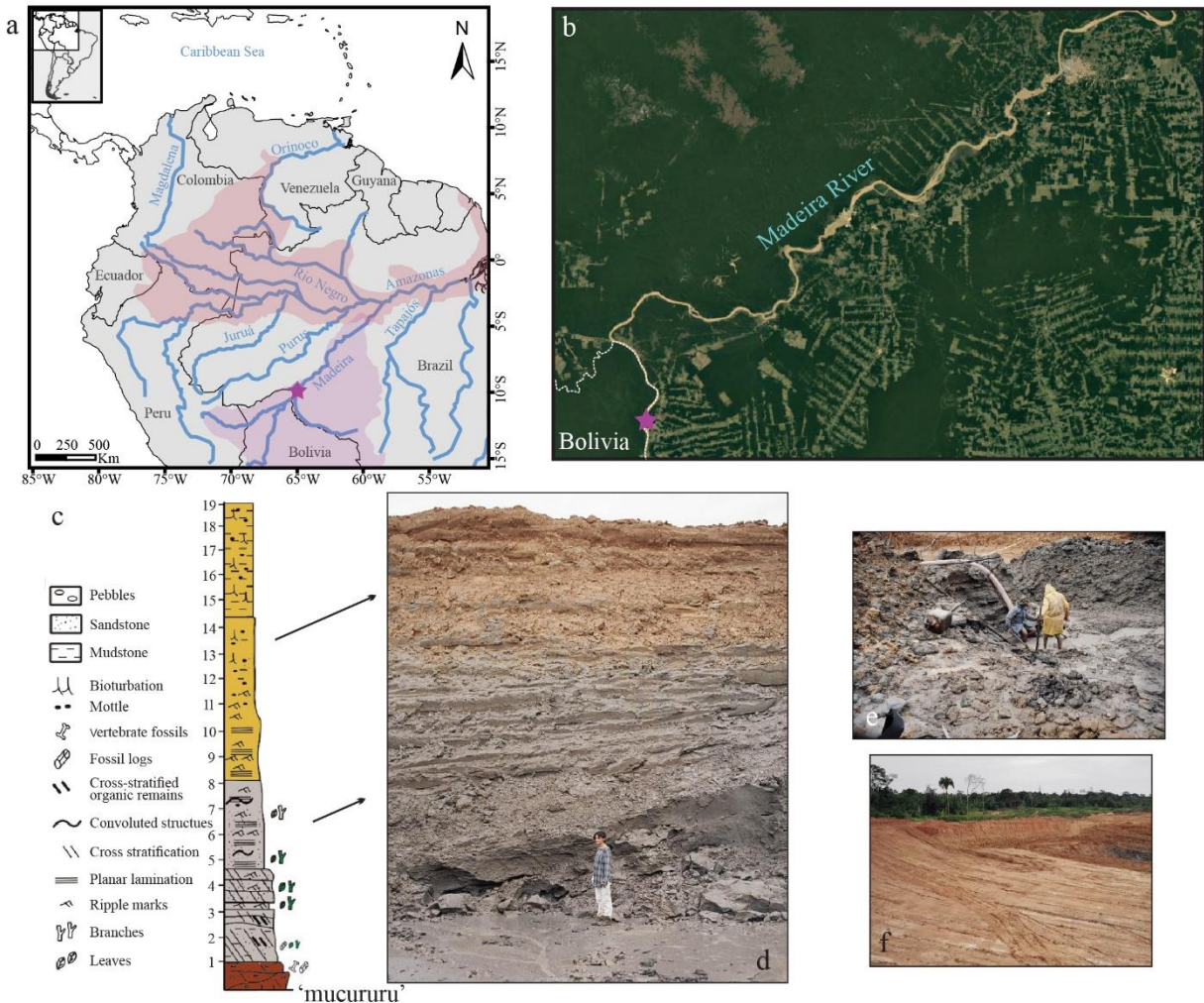
Materials & Methods

Geological context

According to the gold miners that handled MERO.PV.H 007 to E.R.N. in 2009, the specimen was collected two years before at the Taquaras Quarry (9°51'11"S; 65°17'5"W; Supplementary Figure S1), Porto Velho municipality (Rondonia, Brazil), near the border with Bolivia. The collection of the fossil was accidental and done using a dredging machine, thus lacking any stratigraphic context. According to Cozzuol et al. (1), the Taquaras Quarry exposes about 20 m of fluvial deposits, starting with a conglomeratic layer, known as “mucururú”, which is the main auriferous and fossiliferous level of the Late Pleistocene–Holocene Rio Madeira Formation. It can be found in several localities along the Madeira River (1,2), having yielded all vertebrate fossils of the eponymous stratigraphic unit with known stratigraphic provenance (3). In the Taquaras Quarry, the “mucururú” unit is succeeded by greyish conglomeratic sandstones, consolidated by iron oxides and hydroxides, with clay and quartz clasts and plant remains (1), followed by grey cross-stratified sandstones and mudstones. The upper part of the sequence includes yellowish, oxidized mudstones and sandstones, which may be correlated with the Jaci-Paraná Formation (4), a partially younger stratigraphic unit that is more common downstream to the Taquaras Quarry. Rizzotto et al. (5) dated carbonized woods from the “mucururú” as 46,310 to 21,310 years BP, whereas thermoluminescence yielded ages ranging from 130,000 to 9,000 years BP (6). An isolated tooth assigned to *Nechoerus* sp., collected in the same dredging that recovered MERO.PV.H 007, was dated by Asevedo et al. (7) as 29,072–27,713 years BP, which can be corrected for 36,920–36,046 years BP based on the protocol of Dantas et al. (8).

Specimens analysed and measurements

The complete lists of the measurements and specimens sampled for the morphometric and body size datasets are provided in Supplementary Files S2 and S3, respectively. For the morphometric dataset one angular and eight linear measurements were taken from 56 specimens, but one of the measurements (ML) was used only to divide and remove size scaling from the other metrics. For the body size dataset, four linear measurements were taken from 354 specimens (some specimens lack some measurements). A description of each measurement is provided in Supplementary Table S1. The measurements were taken by G.S.F. either manually, using a digital calliper or measuring tape, or digitally from photographs using the software Fiji (9).



Supplementary Figure S1. (a) Map of northwest South America showing distribution of the extant *Peltocephalus dumerilianus* in the Amazon and Orinoco basins (red shaded area) based on Rhodin et al. (10), purple star indicates the Taquara Quarry, type locality of *Pe. maturin* sp. nov. Purple shaded area identifies the Madeira River Basin, in which *Pe. dumerilianus* does not occur today. (b) Satellite zoomed in image of the Madeira River, purple star indicates the Taquara Quarry. (c) Stratigraphic profile of the Taquara Quarry, based on Cozzuol et al. (1). (d-f) Photographs of the Taquara Quarry, (d) exposed middle part of the section, (e) dredging near the base of the section, and (f) top layers.

The specimens are part of the following collections: AMNH, American Museum of Natural History, New York, USA; BMNH, Natural History Museum, London, UK; BSP, Bayerische Staatssammlung für Paläontologie und historische Geologie, Munich, Germany; BSZ, Zoologische Staatssammlung München, Munich, Germany; CRI, Chelonian Research Institute, Oviedo, USA; DGM, Museu de Ciências da Terra, Rio de Janeiro, Brazil; FMNH, Field Museum of Natural History, Chicago, USA; ICN, Instituto de Ciencias Naturales, Universidad Nacional de Colombia, Bogota, Colombia; INPA, Instituto Nacional de Pesquisas da Amazônia, Manaus, Brazil; IVPP, Institute of Vertebrate Paleontology and Paleoanthropology, Beijing, China; MACN, Museo Argentino de Ciencias Naturales, Buenos Aires, Argentina; MCZ, Museum of Comparative

Zoology at Harvard University, Cambridge, USA; MERO, Museu da Memória Rondoniense, Porto Velho, Brazil; MLP, Museo de La Plata, Argentina; MNHN, Muséum national d'Histoire naturelle, Paris, France; MNRJ, Museu Nacional, Rio de Janeiro, Brazil; MPEG, Museu Paraense Emílio Goeldi, Belém, Brazil; MTKD, Staatliches Museum für Tierkunde Dresden, Germany; NMW, National Museum in Warsaw, Poland; PCHP, Peter C. H. Pritchard Collection at the CRI, Oviedo, USA; QM, Queensland Museum, Brisbane, Australia; RH, Ren Hirayama private collection, Japan; SDZ, San Diego Zoo, San Diego, USA; SMF, Senckenberg Naturmuseum Frankfurt, Germany; SMRF, Senckenberg Naturmuseum Frankfurt, Germany; UCMP, University of California Museum of Paleontology, Berkeley, USA; UCMVZ, University of California Museum of Vertebrate Zoology, Berkeley, USA; UF, University of Florida, Gainesville, USA; USNM, Smithsonian National Museum of Natural History, Washington DC, USA; VPPLT, Museo de Historia Natural La Tatacoa, La Victoria, Colombia; ZMB, Museum für Naturkunde Berlin, Germany.

Supplementary Table S1. List and description of the measurements used in this study.

Abbreviation	Description	Unit	Dataset
AJR	angle between the jaw rami	°	morphometric
HC	height at the coronoid process	mm	morphometric
MiL	straight midline length	mm	morphometric & body size
ML	maximal length of the dentary	mm	morphometric
MW	maximum width of the dentaries	mm	morphometric
SH	height of the symphyseal hook	mm	morphometric
TSL	tritulating surface length	mm	morphometric
TSML	tritulating surface midline length	mm	morphometric
TSW	tritulating surface width	mm	morphometric
JL	jaw maximum length	mm	body size
SCm	snout-to-mandibular condyle length	mm	body size
SCL	straight carapace length	mm	body size

Micro-Computed Tomography (μ CT) of extant taxa

In order to compare the dentary morphology of MERO.PV.H 007 with those of extant podocnemidids, specimens of *Erymnochelys madagascariensis* (SMF 7879), *Peltocephalus dumerilianus* (SMF 40168), and *Podocnemis unifilis* (SMF 55470) were scanned with a μ CT Nikon XT H 320 at the 3D Imaging Lab of the Eberhard Karls Universität Tübingen, Germany. The specimens were scanned without filters and using the following parameters: SMF 7879 – voxel

size = 0.034961 mm, energy = 215 kV, current = 18 μ A, projections = 3500; SMF 40168 – voxel size = 0.045918 mm, energy = 190 kV, current = 15 μ A, projections = 4000; SMF 55470 – voxel size = 0.032959 mm, energy = 170 kV, current = 55 μ A, projections = 3500. The dentaries were manually segmented using the brush and lasso tools in Amira (v. 2020.2, ThermoFisher) and surface models were extracted and exported as .stl files. Screenshots were taken using Meshlab v2021.05 (11). All original μ CT datasets and surface models of the specimens used here are openly available on Morphosource (morphosource.org; project ID: 000553087).

Morphometric comparisons and size estimation

Before the morphometric analysis, seven of the eight linear measurements of the morphometric dataset were divided by maximal dentary lateral length (ML) to remove the effect of size scaling, and then log-transformed, generating the final morphometric dataset comprised of one angular and seven unitless log-transformed variables (Supplementary File S4). The dentary morphology of podocnemidids was characterized by plotting the log-transformed measurements and by conducting a Principal Component Analysis (PCA) using the *prcomp* function implemented in R (12) on the morphometric dataset.

An additional dataset was built to estimate the total body size (using straight carapace length, SCL, as a proxy) of *Pe. maturin* using four different variables (Supplementary File S3) taken from 354 specimens. The four variables were analysed using two sets of linear regressions (*lm* function in R): in the first approach (two linear regressions), we estimated SCL from JL, which in turn was estimated using MiL; in the second (three linear regressions), we estimated SCL from SCm, which was estimated from the JL estimates. We obtained best fit, lower, and upper estimates using the function *predict* in R. To consider the cumulative effect of multiple regressions, we used all those three estimates in subsequent predictions. Thus, for example, the final SCL lower bound in the first approach (i.e., using JL), was obtained by using the predicted lower bound of JL in the JL ~ MiL linear regression. This approach inflates the error margins but provides more realistic uncertainty estimates which inevitably result from using multiple regressions.

Ideally, a direct approach (i.e., MiL to SCL) based solely on podocnemidid specimens would be more precise or at least less prone to estimate errors, but two factors prevented us from doing so. First, a restrictive dataset in terms of size range when sample is limited to podocnemidids: MiL vary from 11.1 (*E. madagascariensis*: NMW 139) to 68.95 mm (*Pe. dumerilianus*: CRI 3344) and SCL from 88.99 (NMW 139) to 518.17 mm (*Po. expansa*: NMW 35550) in our dataset, far

below the 266 mm MiL of MERO.PV.H 007, resulting in a very broad confidence interval. Second, when including all Testudines lineages, we introduce a new problem, which is the different allometric relations between body parts that characterises different lineages. We observed that the relative size of the dentary in the lower jaw varies considerably (e.g., (13)), but also the allometric relations between JL or SCm with SCL, spanning to both sides of the relation in podocnemidids (Figure 2b). This suggests that estimates of carapace length for podocnemidids based on this broad dataset of lower jaw or skull measurements is not expected to be much unlike an estimate based on the podocnemidid measurements alone.

¹⁴C Radiocarbon and Stable Isotope Ratio $\delta^{13}\text{C}$ analyses

The hot and humid environment of the Amazon basin complicates the preservation of collagen (14) and, indeed, our geochemical analyses confirmed the absence of this protein in our samples. Thus, to explore the age of MERO.PV.H 007 we submitted three bone samples (UGAMS#48285–7) to the Center for Applied Isotope Studies of the University of Georgia (USA) for radiocarbon dating using bioapatite. The samples were taken from the posterior portion of the dentary, by removing the most superficial layers and scratching the inner portions of the fossilized bone. Bone bioapatite is currently considered to produce measurements as reliable as enamel (15). It is important to note that bioapatite is sensitive to after burial carbon exchange (16) and can yield younger (17) or even older (15) ages, especially in tropical conditions. It is thus necessary to apply particular pretreatment and secondary carbonates removal protocols (14,18) and consider the obtained measurements as approximate, not absolute dates (14,19). We then followed the same protocol as Cherkinsky (18) and Cherkinsky et al. (14), the results of which generally agree with those obtained with other techniques.

Graphite $^{14}\text{C}/^{13}\text{C}$ ratios were measured using a CAIS 0.5 MeV accelerator mass spectrometer. The sample ratios were compared to the ratio measured from the Oxalic Acid I (NBS SRM 4990). The sample $^{13}\text{C}/^{12}\text{C}$ ratios were measured separately using a stable isotope ratio mass spectrometer and expressed as $\delta^{13}\text{C}$ with respect to PDB, with an error of less than 0.1‰. The quoted uncalibrated dates were given in radiocarbon years before 1950 (years BP), using the ^{14}C half-life of 5,568 years. The error is quoted as one standard deviation and reflects both statistical and experimental errors. The date has been corrected for isotope fractionation.

Sampling for spectroscopic analysis

We performed micro-Raman spectroscopy and energy dispersive X-ray fluorescence (EDXRF) analyses to investigate minerals (e.g., carbonates and calcium sulfates) that, according to Cherkinsky (18), may interfere with the reliability of dating from bioapatite. We considered the following samples: (a) fragments of the fossil; and (b) sediments associated with the fossil. These sediments were closely associated with MERO.PV.H 007 and collected by scraping, using magnifying glasses, spatulas, and metal extractors.

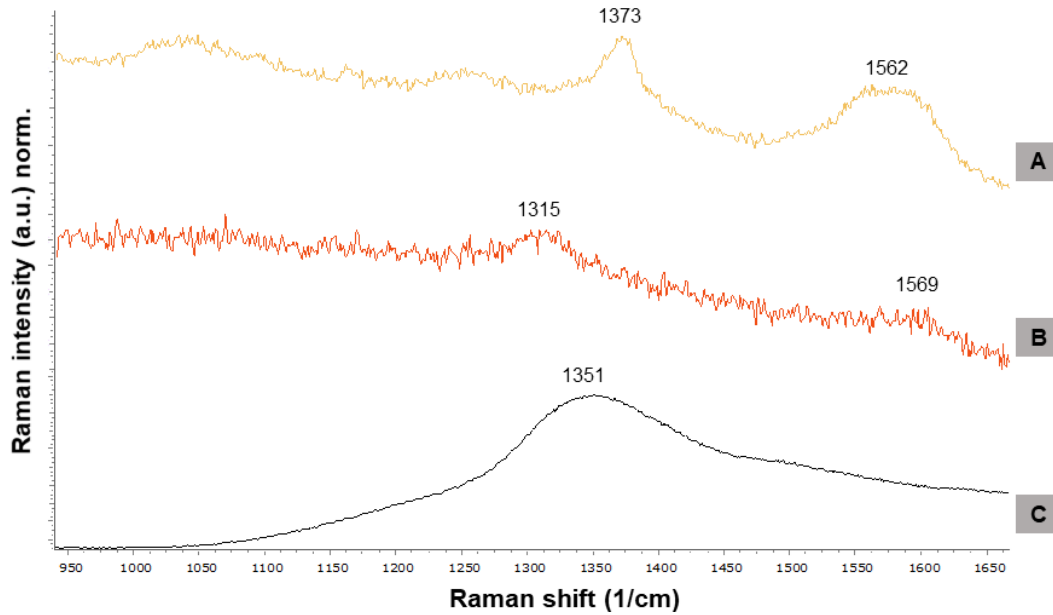
All samples were powdered in an agate mortar until they reached granulometric fractions close to clay. This procedure ensures the interaction of the Raman laser and X-rays beams with greater diversity and types of minerals from different parts of the sample. Because fossil and sediment samples have heterogeneous chemical compositions, the Raman spectra may show overlapping peaks that make it difficult to distinguish minerals and organic matter (OM). Thus, the elements detected by EDXRF helped to identify characteristic peaks in the Raman spectra.

Micro-Raman spectroscopy

We used a Renishaw InVia micro-Raman spectrometer with 532 and 785 nm lasers with the static mode of measurement in order to investigate a broad range of mineral phases and organic matter. Different powers were tested to obtain more informative spectra. We adjusted parameters according to 25mW, using the 5x and LW 50x objectives, with 30 accumulations of two seconds each. We studied the 33 most informative spectra (Supplementary File S5) using the software SpectraGryph 1.2 (20) for the treatment and recognition of Raman peaks and bands. We normalized (0-1) and subtracted the baseline of all spectra, except those referring to the identification of OM, the fluorescence and luminescence effects of which were aggravated with this type of treatment. We searched the *rruff* database and spectra described in scientific articles for comparison with the spectra peaks obtained in our studies.

Energy Dispersive X-ray Fluorescence (EDXRF)

We used a portable EDXRF system by Amptek composed of an X-ray tube in silver (Ag) and a Silicon XR-100SDD FAST detector. Measurements were performed directly on the powdered samples with the 30kV, 5 μ A and time 300s (without collimator). Data fitting was performed using a Windows version of the software system QXAS (WinQXAS 1.4), developed by the International Atomic Energy Agency (IAEA).



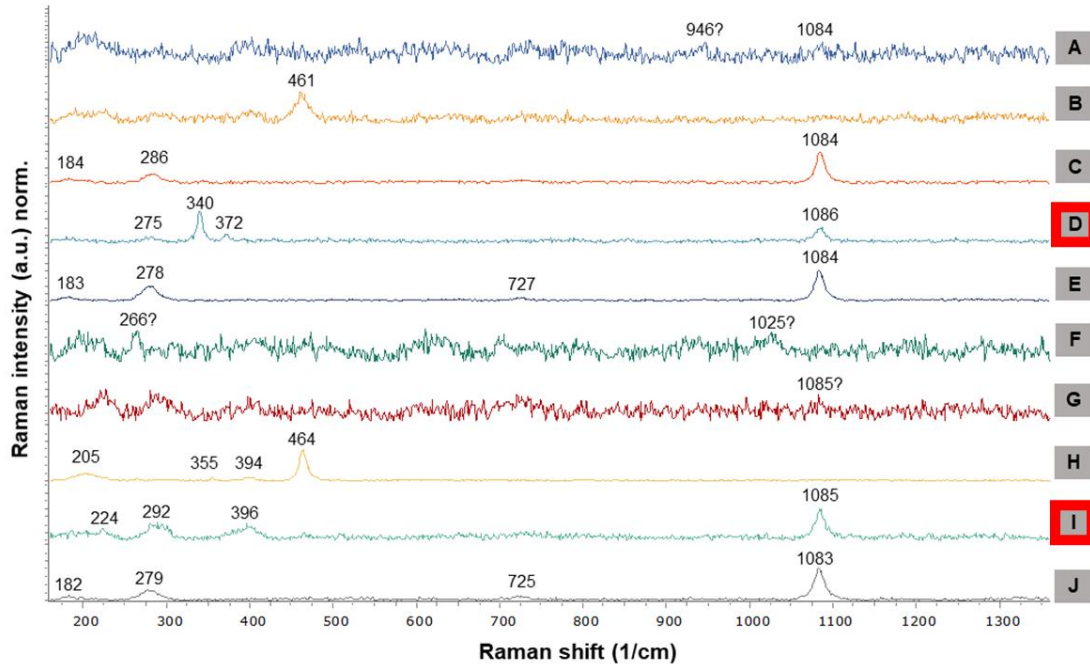
Supplementary Figure S2. Raman spectra from fossil and associated sediment. (a) and (b) sediment spectra. (c) MERO-007 spectrum. Observe D and G bands: 1315 (kerogen or hematite?); 1373 (kerogen); 1562, 1569 (kerogen).

Results

Geochemical and Radiocarbon dating analyses

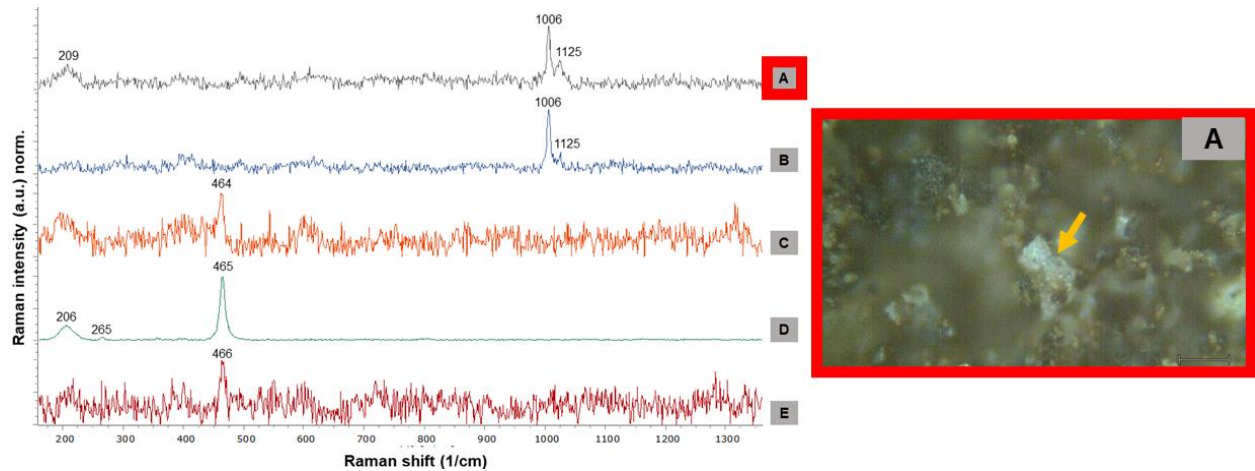
Collagen was not identified in the organic matter content of the samples, so that Nitrogen isotope composition could not be analysed to explore paleodiet or paleoenvironment and the ^{14}C radiocarbon dating was conducted using the bone bioapatite preserved in the fossil. The three samples provided the following ages: $14,290 \pm 45$, $10,070 \pm 45$, and $9,060 \pm 50$ cal BP.

Raman spectroscopy revealed G bands (~ 1562 ; $\sim 1569 \text{ cm}^{-1}$) characteristic of kerogen in sediments associated with different parts of the jaw (Supplementary Figure S2a, b). However, in the bone fragments, we only found the characteristic $\sim 1351 \text{ cm}^{-1}$ peak ; Figure 1C) which tend to overprint in iron-oxidized samples, leading to misidentifications of hematite as a carbon D band (21). We did not detect any other bands (= G) attributable to OM in the fossil. Thus, although suggestive because of the kerogen detected in sediments incrusting bone, it was not possible to corroborate the preservation of OM in the bones.



Supplementary Figure S3. Raman spectra from fossil MERO.PV.H 007. Non identified peaks: ~182-184, 340; quartz: 205, 355, ~394-396; ~461-464; carbonate (calcite and others): ~725-727, ~1083-1086; iron oxyhydroxides: 224, ~275-292, ~372; possible apatite: 946? (D) and (I) spectra of carbonates and respective images.

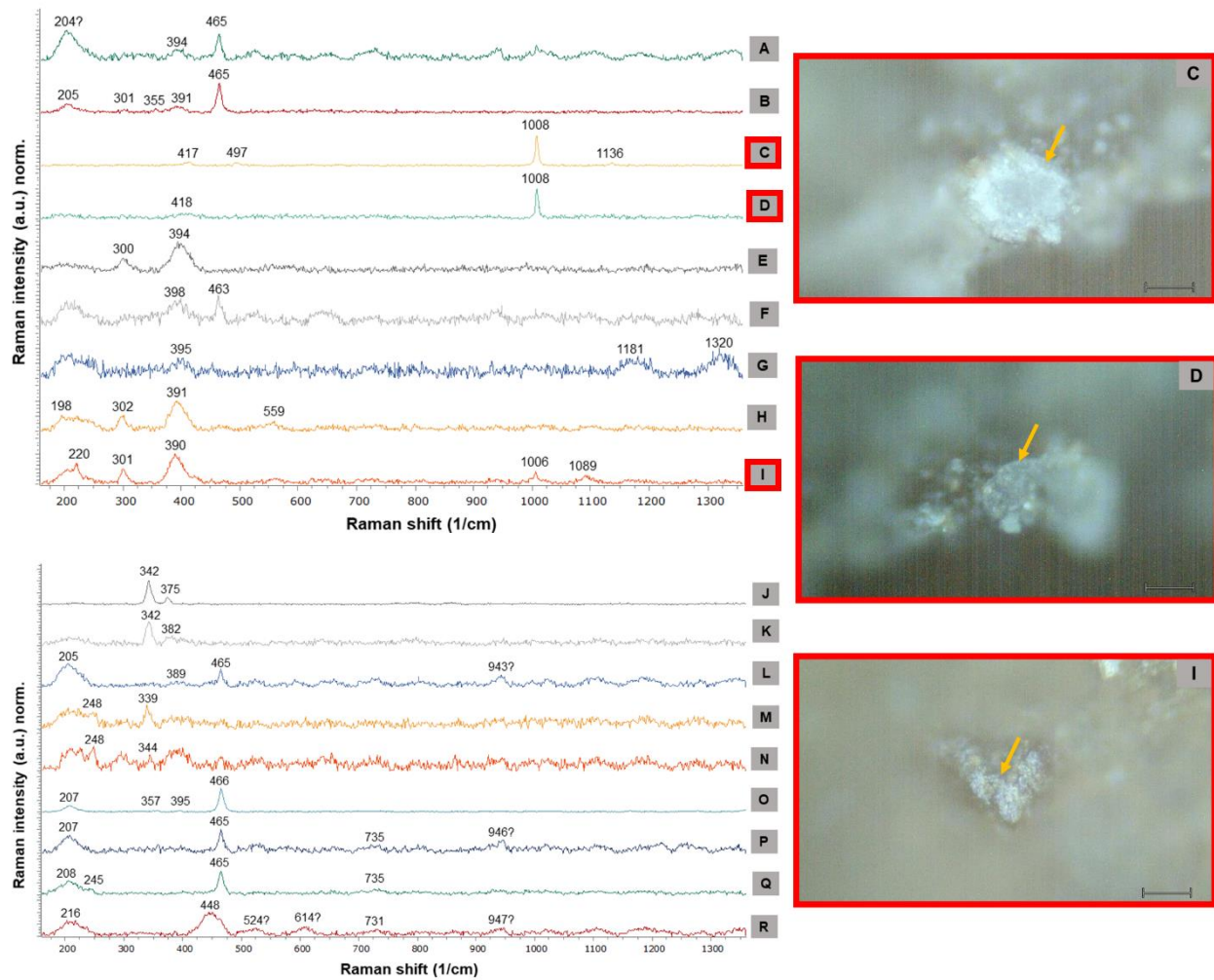
Raman spectra revealed characteristic carbonate, especially calcite peaks ($\sim 725-727$; $\sim 1083-1086 \text{ cm}^{-1}$; Supplementary Figure S3a-e, g-j), with a possible displaced apatite band ($\sim 946 \text{ cm}^{-1}$; Supplementary Figure S3a), in the bone samples. Carbonate minerals were identified by light microscopy (Supplementary Figure S3d, i) and corroborated by EDXRF data (Figure 5), revealing higher counts of calcium in the bone, compared to the associated sediments. However, we did not detect phosphorus in the elemental analyzes on these samples, which reinforces that the possible apatite Raman peak may represent a fluorescence effect.



Supplementary Figure S4. Raman spectra of sediments associated with MERO.PV.H 007. Quartz: ~206-209; ~464-466; gypsum/anhydrite: 1006, 1125. (A) spectrum of gypsum and respective image.

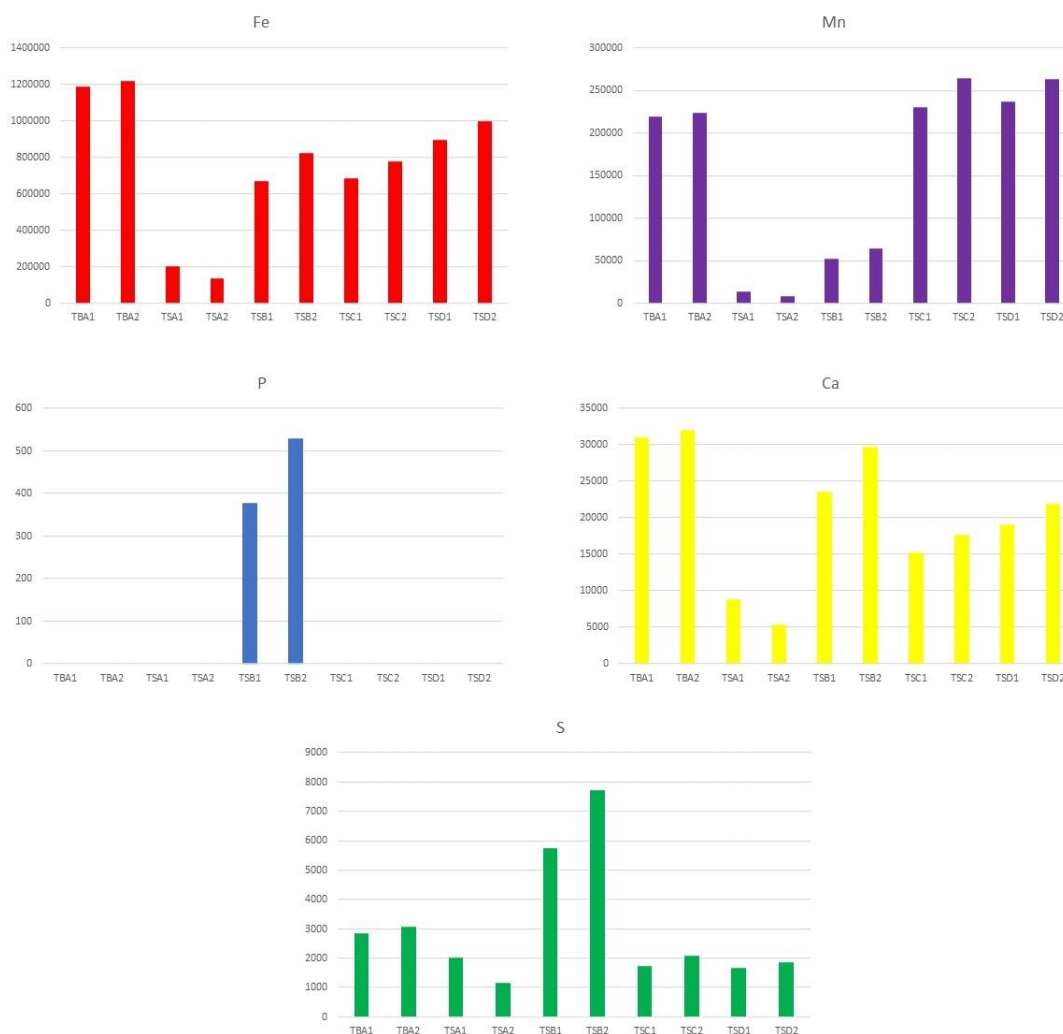
Raman spectra obtained from sediments associated with the fossil showed characteristic peaks of gypsum/anhydrite (~417-418; ~1006-1008 and 1125 cm^{-1}), rare peaks of carbonate (~731-735; 1089 cm^{-1}), and possible apatite peaks (~943-947 cm^{-1} ; Supplementary Figures S4, S5). These data were also corroborated by microscopy (Supplementary Figures S4a, S5c, d, i) and EDXRF (Supplementary Figure S6). The EDXRF methods allowed the identification of S, P, Ca, Fe, Mn, and other chemical elements in the analyzed samples. The bar chart (Supplementary Figure S6) shows the area obtained for each measured element in each EDXRF spectrum. We found considerable counts of phosphorus in the sediments. In some cases, sulfur counts were much higher in the sediments than in the fossil, reinforcing the presence of calcium sulfates. We did not identify gypsum in the bone, but the sulfur counts are very suggestive of the presence of sulfur minerals.

We detected Raman peaks from quartz (~204-208; ~355-357; ~389-398; ~461-466 cm^{-1}) and iron oxyhydroxides (~216-220; ~245-248; 275-292; 300-302; 372; 614; 1.320 cm^{-1}), both in the bone and associated sediments (Supplementary Figures S3-5). Manganese counts obtained by EDXRF were high for both fossil and sediments. We emphasize that the iron counts were much higher in the fossil samples than in the sediment (Supplementary Figure S6). This may derive from a longer exposure time and weathering action on the bones.



Supplementary Figure S5. Raman spectra of sediments associated with MERO.PV.H 007. Quartz: ~ 204 - 208 , ~ 355 - 357 , ~ 389 - 398 , ~ 463 - 466 ; carbonate (calcite and others): ~ 731 - 735 , 1089 ; iron oxyhydroxides: ~ 216 - 220 , ~ 245 - 248 , ~ 300 - 302 , 614 , 1320 ; possible apatite: ~ 943 - 947 ; Zn/Mn oxyhydroxides (?) ~ 524 , 559 ; non identified sulfate: ~ 417 - 418 , 1136 ; non identified peaks: 198 , 1181 (oxides?), 342 , ~ 375 - 382 . (C) and (D) spectra of gypsum and respective images. (I) spectrum of carbonate and respective image.

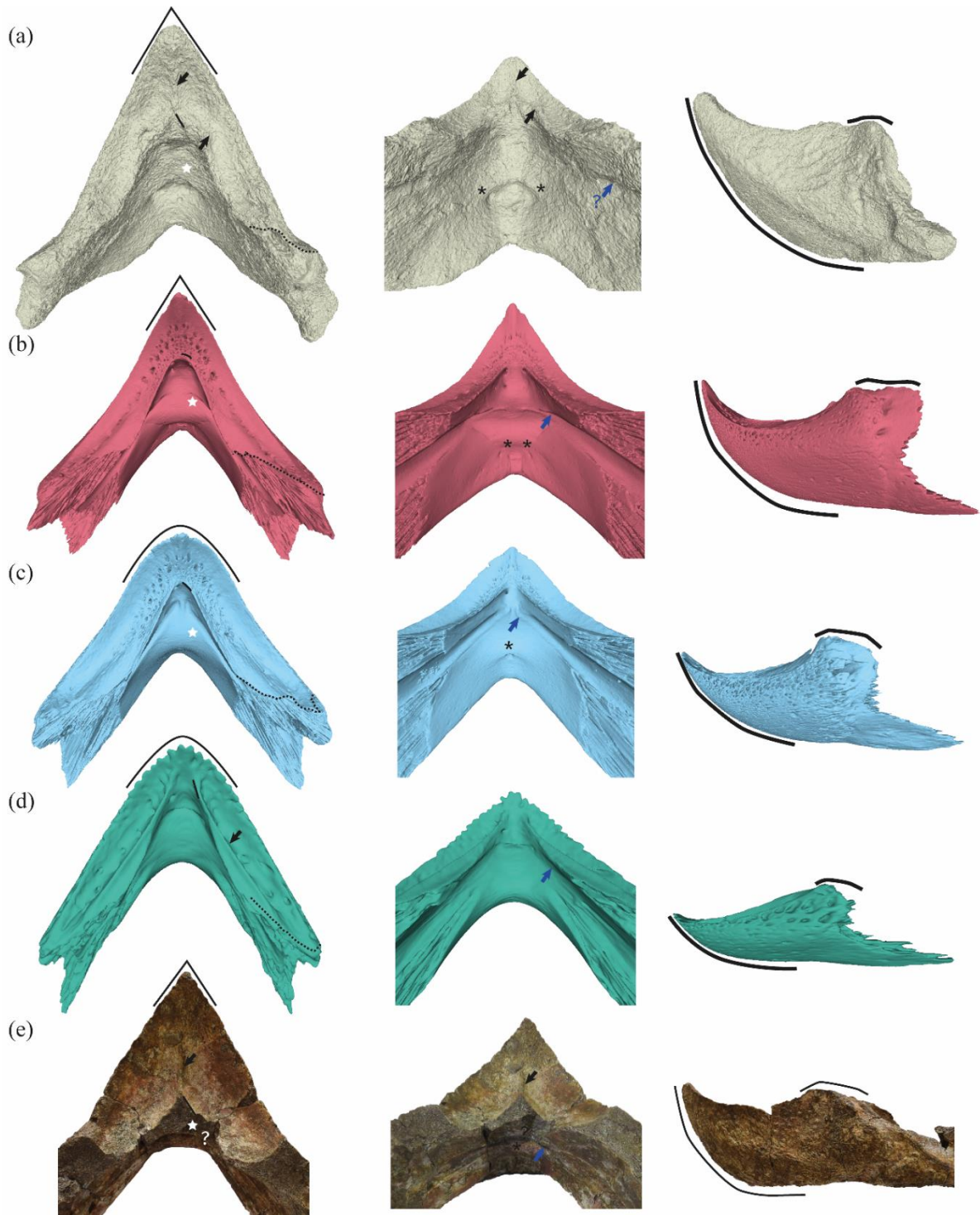
Previous investigations have shown that fossil bones preserved in carbonate-rich environments provide significantly younger bioapatite ages compared to the collagen fraction. This is because, original bioapatite could be replaced by chemical or microbiological exchange with the carbonates in the environment (18).



Supplementary Figure S6. Bar chart of the area (counts) in the EDXRF spectra of some elements for each sample. Note that iron and calcium present higher counts (y axis) in fossil bones in comparison to sediments. Phosphorus was detected only in sediments. Abbreviations: TBA1 e TBA2 – two different acquisitions of the same turtle bone sample (A); TSA1, TSA2, TSB1, TSB2, TSC1, TSC2, TSD1, TSD2 – two different acquisitions for diverse sediment samples (A, B, C, D) associated to turtle jaw. For further details and information on other elements, see the Supplementary File S6.

Summing up, the carbonates detected in the turtle fossil could be from the original bone bioapatite. Yet, it is most likely that it represents diagenetic carbonate and/or the recrystallization of the carbonate apatite in the bone. This is supported by spectroscopic data, such as the high iron counts and the presence of hematite and other iron oxyhydroxides (indicating an intensely weathered, and overall, poorly preserved bone), in addition to the presence of gypsum and carbonate in the associated sediments. In a very weathered bone, calcium carbonates and sulfates from the sediments may have induced the transformation of bone bioapatite into carbonated apatite (22). Similarly, phosphate from bones or sediments may have promoted the phosphatization of

gypsum, resulting in brushite and carbonate apatite (23,24). These dissolution and precipitation reactions may have resulted in the rejuvenation of the radiocarbon age.



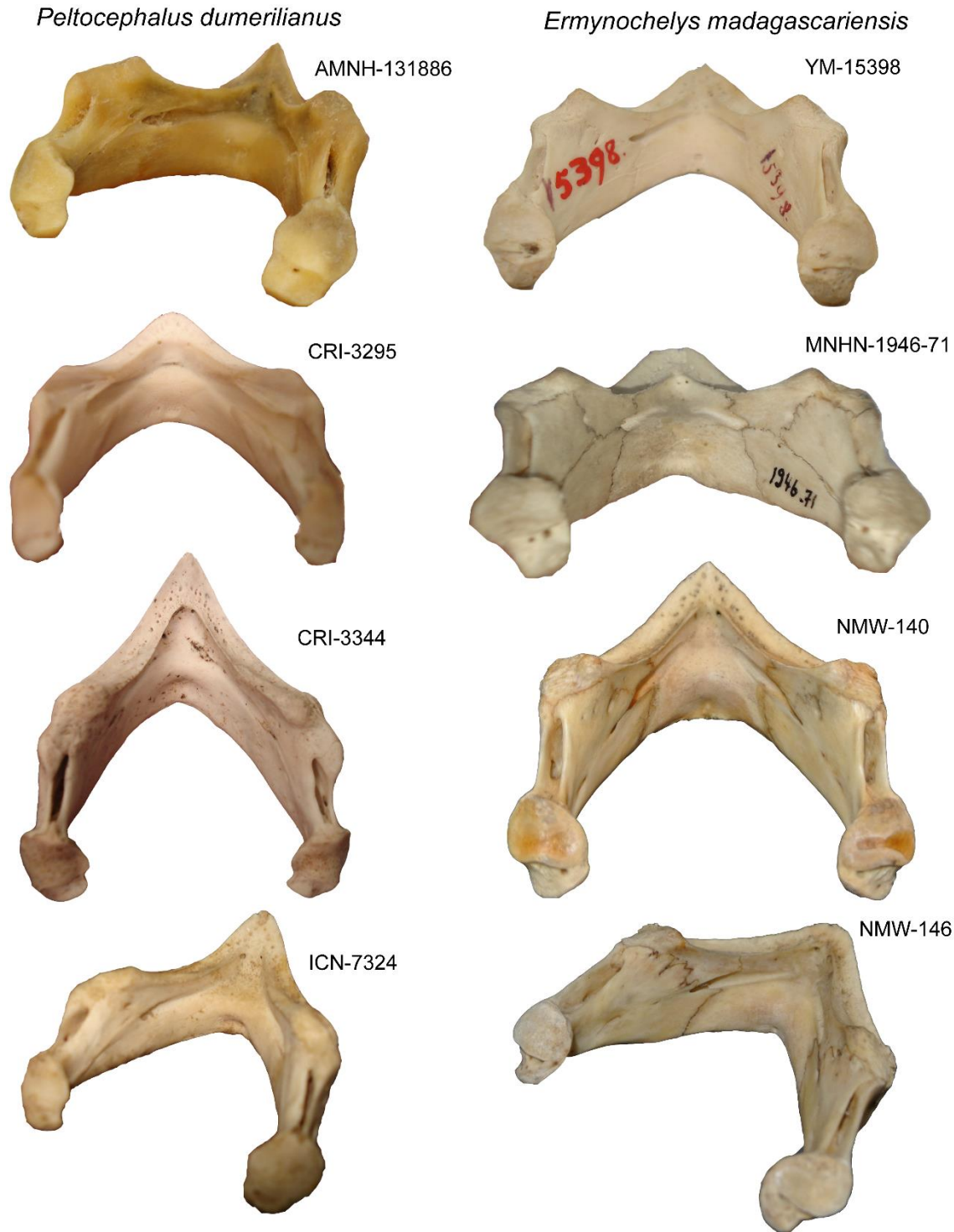
Supplementary Figure S7. Comparison of the dentary bones of selected podocnemidids in dorsal (left), posterior (center) and left lateral (right) views. (a) *Peltocephalus maturin*, (b) *Peltocephalus dumerilianus*, (c) *Erymnochelys madagascariensis*, (d) *Podocnemis unifilis* and (e) *Stupendemys geographica* (VPPLT-979). (a–d) are 3D renderings and (e) are photographs. Solid and dashed lines highlight outlines and sutures, respectively, black arrows point to

ridges and blue arrows to the sulcus cartilaginis meckelii, black asterisks and white stars mark pits and the horizontal shelf in the symphysis.

Comparative Description

Apart from its gigantic size, the uniqueness of *Pe. maturin* among podocnemidids is supported by dentary traits, such as a labial ridge higher than the lingual ridge and a triturating surface separated into anterior and posterior concavities. As in all extant podocnemidids, the dentaries of MERO.PV.H 007 possess clear labial and lingual ridges, which are straight and parallel to one another as in *E. madagascariensis* and *Pe. dumerilianus*, contrasting with the slightly curved lingual ridges of *Podocnemis* spp (Supplementary Figure S7). Although well-defined, the triturating surface in *Pe. dumerilianus* is comparatively shallow. Also, the lingual ridge of MERO.PV.H 007 is hidden by the higher labial ridge in lateral view, whereas in all other crown podocnemidids (Supplementary Figure S7), either the lingual (e.g., *Pe. dumerilianus*, *E. madagascariensis*, and *Stupendemys geographica*; Cadena et al. 2020) or the secondary (e.g., *Podocnemis* spp.) ridge is the highest.

The lingual ridges of MERO.PV.H 007 approach one another anteriorly, forming a sharp angle in dorsal view, as in *E. madagascariensis* and *Podocnemis* spp. and unlike the curved junction seen in *Pe. dumerilianus*. Yet, as in the latter taxon, the ridges meet in the midline, so that the triturating surface has a V-shaped posterior edge. A midline ridge separates the left and right triturating surfaces, as in *Po. vogli* and *Po. lewyana*, but in contrast to all other extant podocnemidids. In *Podocnemis* spp., one or more longitudinal accessory ridges are seen between the labial and lingual ridges, but none of such occurs on the triturating surface of MERO.PV.H 007, *Pe. dumerilianus*, and *E. madagascariensis*. Longitudinal secondary ridges are also known in *Turkanemys pattersoni*, from the Miocene-Pliocene of Kenya (25), and in a lower jaw from the Oligocene of Egypt, referred to *Neochelys fajumensis* (26) or *Dacquemys paleomorpha* (27). On the other hand, MERO.PV.H 007 possesses a low orthogonal ridge dividing the triturating surface into anterior and posterior concavities (Supplementary Figure S7), a unique trait among podocnemidids. This ridge starts medially as an elevation of the lingual ridge and extends orthogonal to the triturating surface long axis.



Supplementary Figure S8. Lower jaws of *Peltocephalus dumerilianus* (right column) and *Erymnochelys madagascariensis* (left column) in posterior or oblique posterior views. Note that the concavity below the lingual platform in *Pe. dumerilianus* is deeper than in *E. madagascariensis*.

The series of small foramina piercing the mandibular triturating surface of *Podocnemis* spp. and *Pe. dumerilianus* cannot be observed in MERO.PV.H 007, but it is unclear whether this is an artefact resulting from the heavy weathering of the specimen, or a trait shared with *E.*

madagascariensis. Although the coronoids are not preserved in MERO.PV.H 007, the suture line between that bone and the dentary can be clearly identified, traversing the triturating surface on a posterolateral to anteromedial direction. Hence, as in all extant podocnemidids, the coronoids contributed to the mandibular triturating surface (Supplementary Figure S7). Also, although less strongly than in extant podocnemidids, the dorsal surface of the MERO.PV.H 007 dentary rises near the coronoid process. The coronoid process in *Podocnemis* spp. and *E. madagascariensis* is commonly higher than the symphyseal hook, whereas the contrary is the case in *Peltocephalus* spp. (Supplementary Figure S7).

The lower jaw symphysis is fused in MERO.PV.H 007 as in all Pelomedusoides. Although the *Podocnemis* species differ in many aspects of their lower jaw anatomy, the dentaries are always lower than those of *Peltocephalus* spp. (Supplementary Figure S7) and lack a dorsally projected symphyseal hook (13). The symphyseal hook in MERO.PV.H 007 is high and upturned, but not as much as in *Pe. dumerilianus*. The anteroventral surface of the symphyseal area is as curved as in *Pe. dumerilianus*, contrasting with the anterodorsally inclined and anteroventrally flattened hook of *Podocnemis* spp. On the posterior surface of the symphyseal area, the lower jaw of *Pe. dumerilianus* forms a flattened horizontal shelf (13) in the midline between the hemimandibles. Although this area is also sturdier than the surroundings in *Podocnemis* spp., the posterior surface of their symphyseal areas forms a continuous slope (Supplementary Figure S7, S8). In MERO.PV.H 007 and *E. madagascariensis* the horizontal shelf it is not as flattened as in *Pe. dumerilianus*, but also not as sloping as in *Podocnemis* spp. Also, a ventral excavation is seen in the posterior surface of the symphyseal area of MERO.PV.H 007, *Pe. dumerilianus*, and *E. madagascariensis*, but not in *Podocnemis* spp. In the same area, two collateral pits pierce the jaw of MERO.PV.H 007 and *Pe. dumerilianus*, but a single central pit is seen in *E. madagascariensis*.

The precise extension of the sulcus cartilaginis meckelii is difficult to determine due to the extensively weathered surface of MERO.PV.H 007. Its posterolateral edges are more easily seen on the right dentary, which also preserves a well-defined foramen alveolare inferius. This foramen opens posteriorly, ventral to the coronoid suture. Aside from these structures, only a very thin line hints at the possibly short anterior extension of the sulcus cartilaginis meckelii, which does not seem to extend as far anteriorly as in *Pe. dumerilianus* and *E. madagascariensis* (Supplementary Figure S7, S8).

Near the contact with the coronoid, the right dentary of MERO.PV.H 007 bears a large lateral perforation anterior to the rhamphotheca scar, which might correspond to the dentofacialis

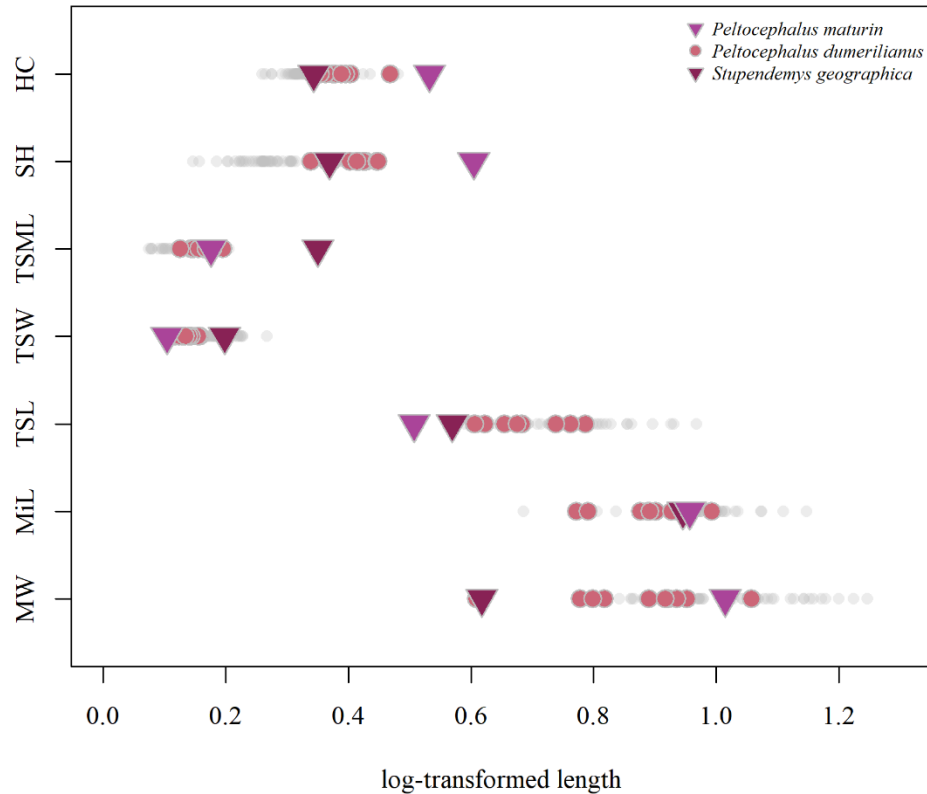
foramen. However, as a similar perforation was not identified on the left side and because that foramen opens posterior to the rhamphotheca scar in all extant podocnemidids, the identified perforation might have been produced by a scavenger. The sulcus that limits the rhamphotheca posteriorly, forming the anterior edge of the podocnemidid jaw scute, extends dorsoventrally in MERO.PV.H 007 (Fig. 1) and *Pe. dumerilianus*, whereas it is anteroventrally to posterodorsally oriented in *Podocnemis* spp. and *E. madagascariensis* (Supplementary Figure S7).

Three giant lower jaws are known from the Miocene fossil record of northern South America: AMU-CURS-706 and VPPLT-979 are assigned to *Stupendemys geographica* (28) and LACM 141498 tentatively referred to *Caninemys tridentata* (28,29). The two specimens of *S. geographica* also show high, sturdy dentaries, forming a pronounced symphyseal hook as in *Pe. maturin*, but can be clearly differentiated from the latter by their broader triturating surface. In addition, the triturating surfaces of AMU-CURS-706 and VPPLT-979 are divided on their midline by a longitudinal ridge and the entire surfaces are longer than that of *Pe. maturin*. Also, the dentary is proportionally longer in *S. geographica* than in both *Peltocephalus* species. The secondary ridge, orthogonal to the long axis of the triturating surface, which divides the *Pe. maturin* surface into anterior and posterior portions, is lacking in *S. geographica*. Moreover, both AMU-CURS-706 and VPPLT-979 show a deep concavity on the posterior end of each triturating surface (Supplementary Figure S7), absent in MERO.PV.H 007. LACM 141498 (30) also possesses the deep posterior concavity and a triturating surface divided by a midline longitudinal ridge. Its dentary is further unlike that of *Pe. maturin* by showing convex, instead of straight, labial ridges, that form a spindle-shaped triturating surface.

Morphospace analysis

Analyses of log-transformed measurements of the lower jaw (Supplementary Figure S9) confirm the morphological distinctiveness between *Pe. maturin* and both *Pe. dumerilianus* (the living species of the genus) and *S. geographica* (the other giant podocnemidid with preserved lower jaws). Although similar regarding the relative midline length of the dentary (MiL) and the triturating surface length (TSL), on all other measurements – especially the maximum width (MW) and the symphysis height (SH) – *Pe. maturin* and *S. geographica* can be clearly set apart (Supplementary Figure S9). In comparison to the extant podocnemidid, the relative values of MiL, MW, and the triturating surface width and midline length (TSW and TSML, respectively) of *Pe. maturin* plot

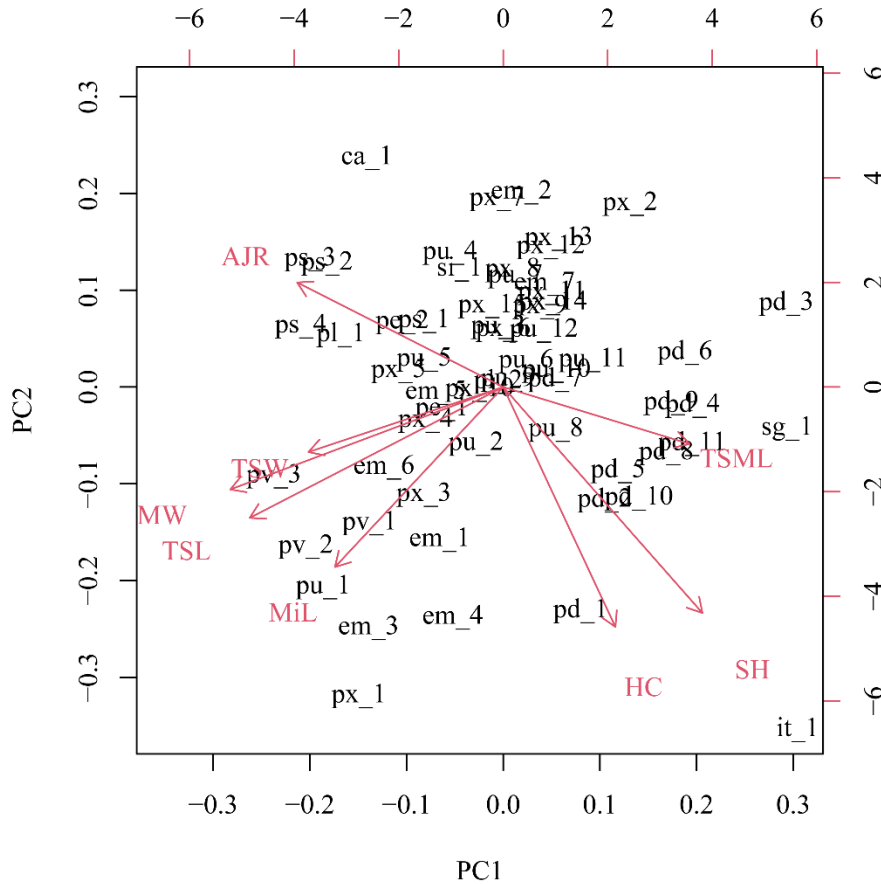
within the range observed for the *Pe. dumerilianus* specimens (Supplementary Figure S9), but the other three parameters discern these taxa.



Supplementary Figure S9. Distribution of log-transformed linear measurements. Abbreviations for the variables can be found in Supplementary Table S1.

The Principal Component Analysis (PCA) also confirm the above distinctions (Fig. 2a). The first two principal components explained 62.14% of the variation (PC1 = 39.88%, PC2 = 22.26%) and are dominated by three sets of measurements (Supplementary Figure S10): positive values of PC1 and negative PC2 scores represent higher HC (height at the coronoid process), SH, and TSML, whereas negative values of PC1 and PC2 are represented by higher MiL, MW, TSL, and TSW. Higher angles between jaw rami (AJR) dominate negative and positive PC1 and PC2 scores, respectively. In the PCA plot (Fig. 2a), *Pe. dumerilianus* specimens plot around more positive PC1 scores than *Podocnemis* spp. and *E. madagascariensis* specimens and on the mid-range of PC2 values. This reflects the sharper angle between hemimandibles, the higher symphyseal hook, and the longer and narrower triturating surface of the lower jaws of *Pe. dumerilianus* relative to those of *Podocnemis* spp. or *E. madagascariensis*, which also characterize

the jaws of *Pe. maturin*. *Podocnemis sextuberculata* and *Po. vogli* are characterized by lower and broader jaws, thus showing the lowest PC1 values, whereas *Pe. dumerilianus* specimens show overall narrower and higher lower jaws. Both *Pe. maturin* and *S. geographica* plot on the right bottom quadrant of the morphospace, with the former differing from the latter mostly by more negative PC2 values (Fig. 2a).



Supplementary Figure S10. Biplot of PC1 and PC2 showing the contributions of each morphological variable to PC scores. Abbreviations for the variables can be found in Supplementary Table S1 and the point labels on Supplementary File S2.

Body size estimation

Our two approaches for estimating carapace length of *Pe. maturin* yielded similar best fitted results, the first 170.4 cm and the second 173.7 cm. Approach 1 was based on two linear regressions: we first predicted lower jaw length (JL) from dentary length (MiL) using equation (1a) obtained from a sample of 39 podocnemidids ($R^2 = 0.9896$; $p < 0.0001$):

$$(1a) \log(JL) = 0.3234 + 0.9718 \times \log(MiL)$$

and then carapace length (SCL) was estimated from JL using equation (1b) ($R^2 = 0.784$, $p < 0.0001$) based on a sample of 219 testudines:

$$(1b) \log(SCL) = 2.2869 + 0.8964 \times \log(JL)$$

Considering the cumulative prediction error (see Material & Methods for full description), the lower bound of Approach 1 was estimated in 140.78 cm and the upper bound in 207.81 cm. Approach 2 included equation (1a) and two additional linear regressions: equation (2a) ($R^2 = 0.9833$; $p < 0.0001$) was used to predict snout-mandibular-condyle length (SCm) from JL:

$$(2a) \log(SCm) = 0.1909 + 0.9906 \times \log(JL)$$

and then SCL was predicted from SCm using equation (2b) ($R^2 = 0.786$; $p < 0.0001$):

$$(2b) \log(SCL) = 2.1058 + 0.9097 \times \log(SCm)$$

The cumulative lower and upper bounds of CML with Approach 2 was 140.74 and 216.98 cm, respectively. Noteworthy, the skull and lower jaw lengths present an isometric relation (slope = 0.99), and a quasi-isometric relation (slope = 0.97) was obtained for dentary and lower jaw lengths. On the other hand, the relation between carapace and the head (slope for lower jaw and skull length, 0.90 and 0.91, respectively) are slightly allometrically negative. Moreover, the R^2 values suggest that in all different groups of extant turtles the relation between dentaries with lower jaws and skulls are similar (0.9896 and 0.9833, respectively), whereas carapace length is explained not as well by lower jaw or skull lengths (78.4% and 78.6%, respectively).

Supplementary References

1. Cozzuol MA, Latrubesse EM, da Silva, S. A. F. Estudo de viabilidade para implementação de usinas hidrelétricas no rio Madeira. Relatório Parcial. Paleontologia. Porto Velho, Brazil: UNIR/RIOMAR/FURNAS; 2004 p. 56.
2. Costa ML. Os Mucururus de Rondônia: considerações mineralógicas e geoquímicas. In: Anais do III Simpósio de Geologia da Amazônia. Belém, Brazil: Sociedade Brasileira de Geologia; 1991. p. 464–78.
3. Holanda E, Cozzuol MA. New records of *Tapirus* from the late Pleistocene of southwestern Amazonia, Brazil. Rev Bras Paleontol. 2006;9(2):193–200.
4. Adamy A, Romanini SJ. Geologia da região de Porto Velho-Abunã. CPRM. 1990;

5. Rizzotto GJ, Cruz NM, Oliveira JG, Quadros MLES, Castro JM. Paleoambiente e o registro fóssilífero pleistocênico dos sedimentos da Formação Rio Madeira. In Belém, Brazil: Sociedade Brasileira de Geologia-Núcleo Norte; 2006.
6. Da-Rosa ÁAS, Leal LA, Pires EF, Sayão JM, Scherer CS, Martello AR, et al. Resultados preliminares do Projeto Executivo do Programa de Investigação, Salvamento e Monitoramento Paleontológico do AHE Jirau. In Boa Vista, Brazil; 2012.
7. Asevedo L, Ranzi A, Kalliola R, Pärssinen M, Ruokolainen K, Cozzuol MA, et al. Isotopic paleoecology ($\delta^{13}\text{C}$, $\delta^{18}\text{O}$) of late Quaternary herbivorous mammal assemblages from southwestern Amazon. *Quat Sci Rev.* 2021;251:106700.
8. Dantas MAT, Gomes VS, Cherkinsky A, Araújo-Junior HI de. Annual isotopic diet ($\delta^{13}\text{C}$) of *Erethotherium laurillardii* (Lund, 1842) and climate variation ($\delta^{18}\text{O}$) through the late Pleistocene in the Brazilian Intertropical Region. *Quat Res.* 2023;1–8.
9. Schindelin J, Arganda-Carreras I, Frise E, Kaynig V, Longair M, Pietzsch T, et al. Fiji: an open-source platform for biological-image analysis. *Nat Methods.* 2012;9(7):676–82.
10. Rhodin AGJ, Iverson JB, Bour R, Fritz U, Georges A, Shaffer HB, et al. Turtles of the World: Annotated Checklist and Atlas of Taxonomy, Synonymy, Distribution, and Conservation status. In: Rhodin AGJ, Iverson JB, Van Dijk PP, Stanford CB, Goode EV, Buhlmann K, et al., editors. *Conservation Biology of Freshwater Turtles and Tortoises: a Compilation Project of the IUCN/SSC Tortoise and Freshwater Turtle Specialist Group* [Internet]. 9th ed. Chelonian Research Foundation and Turtle Conservancy; 2021 [cited 2023 Aug 23]. (Chelonian Research Monographs; vol. 8). Available from: <https://iucn-tftsg.org/checklist/>
11. Cignoni P, Callieri M, Corsini M, Dellepiane M, Ganovelli F, Ranzuglia G. MeshLab: an Open-Source Mesh Processing Tool. In: Scarano V, Chiara RD, Erra U, editors. *Eurographics Italian Chapter Conference*. The Eurographics Association; 2008.
12. R Core Team. R: A language and environment for statistical computing [Internet]. Vienna, Austria: R Foundation for Statistical Computing; 2022. Available from: <https://www.R-project.org/>
13. Evers SW, Ponstein J, Jansen MA, Gray JA, Fröbisch J. A systematic compendium of turtle mandibular anatomy using digital dissections of soft tissue and osteology. *Anat Rec.* 2023;306(6):1228–303.
14. Cherkinsky A, Dantas MAT, Cozzuol MA. Bioapatite ^{14}C Age of Giant Mammals from Brazil. *Radiocarbon.* 2013;55(2):464–71.
15. Zazzo A. Bone and enamel carbonate diagenesis: A radiocarbon prospective. *Palaeogeogr Palaeoclimatol Palaeoecol.* 2014;416:168–78.
16. Wright DK. Accuracy vs. Precision: Understanding Potential Errors from Radiocarbon Dating on African Landscapes. *Afr Archaeol Rev.* 2017;34(3):303–19.
17. Zazzo A, Saliège JF. Radiocarbon dating of biological apatites: A review. *Palaeogeogr Palaeoclimatol Palaeoecol.* 2011;310(1):52–61.
18. Cherkinsky A. Can We Get a Good Radiocarbon Age from “Bad Bone”? Determining the Reliability of Radiocarbon Age from Bioapatite. *Radiocarbon.* 2009;51(2):647–55.

19. Zazzo A, Munoz O, Saliège JF. Diet and mobility in a late neolithic population of coastal oman inferred from radiocarbon dating and stable isotope analysis. *Am J Phys Anthropol.* 2014;153(3):353–64.
20. Menges F. Spectragryph Optical Spectroscopy Software, Version 1.2. 14. Oberstd Ger 2019 Available Online <https://www.effemm2.de/spectragryph>. 2020;
21. Brolly C, Parnell J, Bowden S. Raman spectroscopy: Caution when interpreting organic carbon from oxidising environments. *Planet Space Sci.* 2016;121:53–9.
22. Ana ID, Matsuya S, Ishikawa K. Engineering of carbonate apatite bone substitute based on composition-transformation of gypsum and calcium hydroxide. *Engineering.* 2010;02(05):344–52.
23. Pinto AJ, Jimenez A, Prieto M. Interaction of phosphate-bearing solutions with gypsum: Epitaxy and induced twinning of brushite (CaHPO₄·2H₂O) on the gypsum cleavage surface. *Am Mineral.* 2009;94(2–3):313–22.
24. Altundal S, Laurenti M, López-Cabarcos EJ, Rubio-Retama J, Gross KA. Accelerated transformation of brushite cement into carbonate apatite in biomimetic solution. *Key Eng Mater.* 2019;800:70–4.
25. Wood RC. Fossil Turtles from Lothagam. In: Leakey MG, Harris JM, editors. Lothagam [Internet]. Columbia University Press; 2003 [cited 2023 Aug 24]. p. 115–36. Available from: <https://www.degruyter.com/document/doi/10.7312/leak11870-007/html>
26. Andrews CW. A descriptive catalogue of the Tertiary Vertebrata of the Fayum, Egypt. Order of the Trustees of the British Museum; 1906.
27. Williams E. New or redescribed pelomedusid skulls from the Tertiary of Africa and Asia (Testudines, Pelomedusidae). 2. A Podocnemididae skull from the Miocene of Moghara, Egypt. *Breviora.* 1954;39:1–8.
28. Cadena EA, Scheyer TM, Carrillo-Briceño JD, Sánchez R, Aguilera-Socorro OA, Vanegas A, et al. The anatomy, paleobiology, and evolutionary relationships of the largest extinct side-necked turtle. *Sci Adv.* 2020;6(7):eaay4593.
29. Meylan PA, Gaffney ES, Campos D de A. Caninemys, a new side-necked turtle(Pelomedusoides, Podocnemididae) from the Miocene of Brazil. *Am Mus Novit.* 2009;3639:1–26.
30. Gaffney ES, Campbell KE, Wood RC. Pelomedusoid side-necked turtles from late Miocene sediments in southwestern Amazonia. *Am Mus Novit.* 1998;3245:1–11.